

Validation of flexible multibody dynamics beam formulations using benchmark problems

Olivier A. Bauchau¹ · Peter Betsch² · Alberto Cardona³ ·
Johannes Gerstmayr⁴ · Ben Jonker⁵ ·
Pierangelo Masarati⁶ · Valentin Sonneville⁷

Received: 26 February 2015 / Accepted: 29 February 2016
© Springer Science+Business Media Dordrecht 2016

Abstract As the need to model flexibility arose in multibody dynamics, the floating frame of reference formulation was developed, but this approach can yield inaccurate results when elastic displacements becomes large. While the use of three-dimensional finite element formulations overcomes this problem, the associated computational cost is overwhelming. Consequently, beam models, which are one-dimensional approximations of three-dimensional elasticity, have become the workhorse of many flexible multibody dynamics codes. Numerous beam formulations have been proposed, such as the geometrically exact beam formulation or the absolute nodal coordinate formulation, to name just two. New solution strategies have been investigated as well, including the intrinsic beam formulation or the DAE approach. This paper provides a systematic comparison of these various approaches, which will be assessed by comparing their predictions for four benchmark problems. The first problem is the Princeton beam experiment, a study of the static large displacement and rotation behavior of a simple cantilevered beam under a gravity tip load. The second problem, the four-bar mechanism, focuses on a flexible mechanism involving beams and revolute joints. The third problem investigates the behavior of a beam bent in its plane of greatest flexural rigidity, resulting in lateral buckling when a critical value of the transverse load is reached. The last problem investigates the dynamic stability of a rotating shaft. The predictions of eight independent codes are compared for these four benchmark problems and are found to be in close agreement with each other and with experimental measurements, when available.

✉ O.A. Bauchau
obauchau@umd.edu

¹ University of Maryland, College Park, MD, USA

² Karlsruhe Institute of Technology, Karlsruhe, Germany

³ CIMEC (UNL/Conicet), Santa Fe, Argentina

⁴ Leopold-Franzens Universität Innsbruck, Innsbruck, Austria

⁵ University of Twente, Enschede, The Netherlands

⁶ Politecnico di Milano, Milano, Italy

⁷ Université de Liège, Liège, Belgium

Keywords Multibody dynamics · Beam models · Benchmark problems

1 Introduction

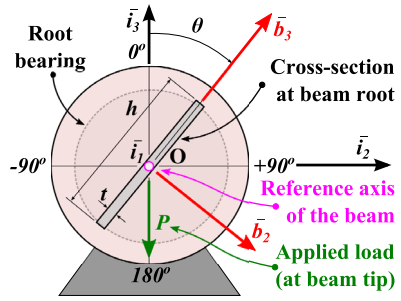
Multibody dynamics was originally developed to deal with simple tree-like topologies composed of rigid bodies. As the need to model flexibility arose, the floating frame of reference formulation [1] was proposed. Unfortunately, as the magnitude of the elastic displacements increases, this formulation becomes increasingly inaccurate, and the multibody dynamics community began to turn its attention to finite element based formulations. Simo [2] proposed the geometrically exact beam formulation (GEBF), which corrected the shortcomings of earlier co-rotational formulations [3]. In recent years, the absolute nodal coordinate formulation (ANCF) developed by Shabana et al. [4, 5] has received considerable attention for the modeling of flexible multibody systems. The GEBF and ANCF are easier to derive than the floating frame of reference approach and involve fewer assumptions, but little effort has been devoted to the systematic comparison of these two approaches.

Romero [6] has presented a comparison of both qualitative and quantitative aspects of the two approaches. He concluded that the ANCF is more straightforward, while GEBF involves thorny issues, such as the treatment of finite rotation. Unfortunately, the ANCF suffers from a number of locking mechanisms that must be eliminated to obtain accurate results. As pointed out by Gerstmayr et al. [7], this can be accomplished in a number of ways, but the proposed techniques complicate the description of elastic forces, leading to more arduous implementations and moving away from the simplicity of the initial implementation. In some of the examples treated by Romero, the ANCF and GEBF did not converge to the same solution. In all cases, the computational efficiency of the GEBF was found to be superior to that of the ANCF.

Bauchau et al. [8] further compared the GEBF and ANCF to identify the causes of their differing computational efficiencies. First, they performed a kinematic analysis in which the exact nodal displacements were prescribed and the predicted displacement and strain fields were compared for the two methods. The accuracies of the predicted strain fields were found to differ markedly: the predictions of the GEBF were more accurate than those of the ANCF. They attributed this phenomenon to the fact that the curvature field is obtained as a second derivative of the displacement in the ANCF, but as a first derivative only for the GEBF. Next, they carried out a static analysis to determine the solution of the problem. For the GEBF, the predictions of the static analysis are far more accurate than those obtained from the kinematic solution; in contrast, the same order of accuracy was obtained for the two solution procedures when using ANCF. In all cases, they reported that the predictions of the GEBF were more accurate than those of the ANCF. A further study by Bauchau et al. [9] compared the predictions of the two methodologies against experimental measurements.

Besides these various formulations of beam problems, novel solution strategies have also been investigated. For instance, Hegemier [10] and Hodges [11] have developed intrinsic formulations for beams. By eliminating the displacement and rotation fields from the geometrically exact equations of the problem, quadratic equations result and this feature simplifies the solution process. Cardona and Géradin [12] adapted the well known Hilber–Hughes–Taylor [13] time integration scheme initially developed for the finite element method to the finite rotation problems found in geometrically exact beams. Betsch and co-workers [14] proposed the use of the direction cosine matrix to represent the rotation tensor; this led to differential-algebraic equations (DAE), which they solved using novel integration techniques. Finally, it is worth mentioning the increased application of Lie group techniques in

Fig. 1 Configuration of the Princeton beam experiment



rigid and flexible multibody dynamics [15]. The resulting solution techniques aim at preserving the invariant manifolds that characterize multibody systems.

2 The four benchmark problems

This study focuses on four benchmark problems: the Princeton beam experiment, the four-bar mechanism, the lateral buckling of a beam, and the stability of a rotating shaft described in Sects. 2.1, 2.2, 2.3, and 2.4, respectively. For each benchmark problem, beam sectional properties such as bending, shearing, and torsional stiffnesses must be evaluated. In this effort, these properties were computed from the section’s geometric and stiffness properties using the procedure developed by Bauchau and Han [16, 17].

2.1 The Princeton beam experiment

The Princeton beam experiment [18, 19] is a study of the large displacement and rotation behavior of a simple cantilevered beam under a gravity tip load. A straight aluminum (T 7075) beam of length $L = 0.508$ m with a rectangular cross-section of thickness $t = 3.175$ mm and height $h = 12.7$ mm was cantilevered at its root and subjected to a static concentrated transverse load P at its tip.

Figure 1 shows an end-view of the test set-up. An inertial frame of reference is selected as $\mathcal{F}^I = [O, \mathcal{I} = (\bar{i}_1, \bar{i}_2, \bar{i}_3)]$ and material frame $\mathcal{F}^B = [O, \mathcal{B} = (\bar{b}_1, \bar{b}_2, \bar{b}_3)]$ is attached at the beam’s root section, which is cantilevered into a bearing that allows rotation of the beam about its reference axis by an angle θ , called the “loading angle.” The gravity load applied at the beam tip is acting in the opposite direction of unit vector \bar{i}_3 . Variation of the loading angle from 0 to 90 degrees yields a range of nonlinear problems where torsion and bending in two directions are coupled.

Experimental results [18] consist of measurements of the beam’s tip deflection along the material unit vectors \bar{b}_2 and \bar{b}_3 , denoted u_2 and u_3 , respectively, and called the “flap-wise” and “chordwise displacements,” respectively. The beam’s tip twist was also measured. Let $\underline{R}^E = \{\bar{b}_1^E, \bar{b}_2^E, \bar{b}_3^E\}$ denote the rotation tensor characterizing the orientation of the beam’s tip cross-section. In the absence of tip load, $\underline{R}^E(P = 0) = \{\bar{b}_1^E, \bar{b}_2^E, \bar{b}_3^E\}$, where $\bar{b}_3^{ET} = \{0, \sin \theta, \cos \theta\}$, and it then follows that $\theta = \arctan(R_{23}^E(P = 0)/R_{33}^E(P = 0))$, where the subscripts refer to the corresponding entries of rotation tensor \underline{R}^E . Under tip load P , the orientation of the tip section is defined as $\arctan(R_{23}^E(P)/R_{33}^E(P))$ and the beam’s tip twist is defined as

$$\phi = \arctan\left(\frac{R_{23}^E}{R_{33}^E}\right) - \theta. \tag{1}$$

Table 1 Sectional stiffness properties of the Princeton beam

	Axial S [MN]	Shearing K_{22} [MN]	Shearing K_{33} [MN]	Torsional H_{11} [N m ²]	Bending H_{22} [N m ²]	Bending H_{33} [N m ²]
Beam	2.842	0.6401	0.9039	3.103	36.28	2.429

The procedure used to measure the twist angle experimentally is detailed in the report by Dowell and Traybar [18].

Data was acquired at loading angles of $\theta = 0, \pm 15, \pm 30, \pm 45, \pm 60, \pm 75, \pm 90$, and 180 degrees. For a perfect system, symmetry implies that the absolute values of the tip displacements and twist should be identical for loading angles $\pm\theta$. In the experimental setting, these measurements differed, providing an estimate of their accuracy. Three loading conditions were used, $P_1 = 4.448$ N, $P_2 = 8.896$ N, and $P_3 = 13.345$ N.

The linear solution of the problem is found using the shear deformable beam theory described in structural analysis textbooks [20]. The tip transverse displacements are

$$u_2^T = \left[\frac{PL^3}{3H_{33}} + \frac{PL}{K_{22}} \right] \sin\theta, \quad u_3^T = \left[\frac{PL^3}{3H_{22}} + \frac{PL}{K_{33}} \right] \cos\theta, \quad (2)$$

where H_{22} and H_{33} are the bending stiffnesses about material unit vectors \bar{b}_2 and \bar{b}_3 , respectively, and K_{22} and K_{33} the shearing stiffnesses along the same unit vectors, respectively. Of course, for linear theory, the tip twist vanishes.

For $\theta = 0$ or 180 and $\theta = \pm 90$, the beam undergoes planar deformation and elementary formulæ of Timoshenko beam theory (2) provide the tip deflection in the linear regime. Using the Young's modulus of T 7075 aluminum as $E = 71.7$ GPa and Poisson's ratio $\nu = 0.31$, hand calculations yield $u_2^T = 5.004$ and $u_3^T = 80.034$ mm for the chordwise and flapwise tip displacements, respectively, at loading level P_1 . This compares favorably with experimental measurements of $u_2^T = 5.3594$ and $u_3^T = 77.635$ mm, respectively, resulting in -6.6% and $+3.1\%$ error, respectively. In this effort, the dimensions of the cross-section were adjusted slightly to achieve good correlation between measurements and predictions of linear theory in these two cases. The following data was used: $L = 0.508$ m, $t = 3.2024$ mm, $h = 12.377$ mm, $E = 71.7$ GPa, $\nu = 0.31$, and $G = E/2(1 + \nu) = 27.37$ GPa. These physical properties translate to the sectional stiffness properties listed in Table 1 and the sectional mass properties per unit span is $m_{00} = 0.1062$ kg/m.

2.2 The four-bar mechanism

Figure 2 depicts a flexible four-bar mechanism. Bar 1 is of length 0.12 m and is connected to the ground at point **A** by means of a revolute joint. Bar 2 is of length 0.24 m and is connected to bar 1 at point **B** with a revolute joint. Finally, bar 3 is of length 0.12 m and is connected to bar 2 and the ground at points **C** and **D**, respectively, by means of two revolute joints.

In the reference configuration, the bars of this planar mechanism intersect each other at 90 degree angles and the axes of rotation of the revolute joints at points **A**, **B**, and **D** are normal to the plane of the mechanism. To simulate an initial defect of the mechanism, the axis of rotation of the revolute joint at point **C** is rotated by $+5$ degrees about unit vector \bar{i}_2 indicated in Fig. 2. The angular velocity of bar 1 at point **A** is prescribed as $\Omega = 0.6$ rad/s for the duration of the simulation.

Bars 1 and 2 are of square cross-section of size 16 by 16 mm; bar 3 has a square cross-section of size 8 by 8 mm. The three bars are made of steel, whose mechanical characteristics

Fig. 2 Configuration of the four-bar mechanism

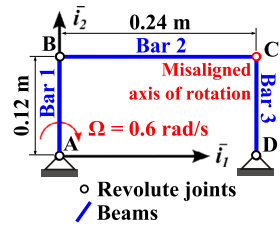


Fig. 3 Configuration of the crank actuated beam

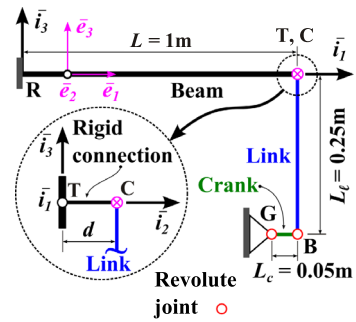


Table 2 Sectional stiffness properties of the bars

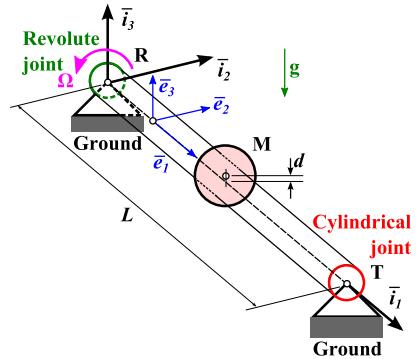
	Axial S [MN]	Shearing K_{22} [MN]	Shearing K_{33} [MN]	Torsional H_{11} [N·m ²]	Bending H_{22} [N·m ²]	Bending H_{33} [N·m ²]
Bars 1 & 2	52.99	16.88	16.88	733.5	1131	1131
Bar 3	13.25	4.220	4.220	45.84	70.66	70.66

are Young’s modulus $E = 207$ GPa and Poisson’s ratio $\nu = 0.3$. These physical properties translate to the sectional stiffness properties listed in Table 2. The sectional mass properties are as follows: mass per unit span $m_{00} = 1.997$ and 0.4992 kg/m, moments of inertia per unit span $m_{22} = m_{33} = 42.60$ and 2.662 mg m²/m for bars 1 and 2, and bar 3, respectively.

If the bars were infinitely rigid, no motion would be possible because the mechanism locks. For elastic bars, motion becomes possible, but generates large, rapidly varying internal forces and moments. If the axes of rotation of the four revolute joints were orthogonal to the plane of the mechanism, the response of the system would be purely planar, and bars 1 and 3 would rotate at constant angular velocity about points **A** and **D**, respectively. The initial defect in the mechanism causes a markedly different response. Bar 1 rotates at the constant prescribed angular velocity, but bar 3 now oscillates back and forth, never completing an entire revolution.

2.3 Lateral buckling of a thin beam

If a beam is bent in its plane of greatest flexural rigidity, lateral buckling will occur when a critical value of the transverse load is reached. In this benchmark problem, the tip of a beam is subjected to a transverse load applied through a crank and link mechanism, as depicted in Fig. 3. The beam is clamped at one end, while the other end is connected to the link through a spherical joint. The crank and link are modeled by flexible beams connected by revolute

Fig. 4 Configuration of the rotating shaft**Table 3** Sectional stiffness properties of the beams

	Axial S [MN]	Shearing K_{22} [MN]	Shearing K_{33} [MN]	Torsional H_{11} [N m^2]	Bending H_{22} [N m^2]	Bending H_{33} [N m^2]
Beam	73	5.025	23.40	877.2	60,830	608.3
Link	33.02	10.81	10.81	914.5	1189	1189
Crank	132.1	43.22	43.22	14,630	19,020	19,020

joints. As the crank rotates, the beam tip is pushed up. When the buckling load is reached, the beam snaps laterally and becomes significantly softer in bending due to the pronounced twisting deformation.

Figure 3 depicts the configuration of the problem. The beam is of length $L = 1$ m, the crank and link lengths are $L_c = 0.05$ m and $L_\ell = 0.25$ m, respectively. The rotation of the crank is prescribed as $\phi = \pi(1 - \cos \pi t/T)/2$, for $t \leq T$ and $\phi = \pi$ for $t > T$, where $T = 0.4$ s. To simulate an initial imperfection of the system, the tip of the beam is connected to the spherical joint via a rigid-body connection of length $d = 0.1$ mm. The plane of the crank and link mechanism is offset from the plane of the beam by the same distance d .

The beam's rectangular cross-section is of width $b = 10$ mm and height $h = 100$ mm. The link has a circular cross-section of radius $R_\ell = 12$ mm. Finally, the crank also features a circular cross-section, but its radius is $R_c = 24$ mm. All components are made of aluminum, whose mechanical characteristics are Young's modulus $E = 73$ GPa and Poisson's ratio $\nu = 0.3$. These physical properties translate to the sectional stiffness properties listed in Table 3. The sectional mass properties are as follows: mass per unit span $m_{00} = 2.68, 1.212$, and 4.85 kg/m, moments of inertia per unit span $m_{22} = 2233, 43.65$, and 698.3 , $m_{33} = 22.33, 43.65$, and 698.3 $\text{mg m}^2/\text{m}$ for the beam, link, and crank, respectively.

2.4 Stability of a rotating shaft

A flexible shaft of length L is supported at its ends by bearings, as depicted in Fig. 4. At point **R**, the shaft is connected to the ground by means of a revolute joint and the angular speed of the shaft is a prescribed function of time, $\Omega(t)$. At point **T**, the shaft is connected to the ground via a cylindrical joint. A rigid disk is attached to the shaft at its mid-span point **M**. Initially, the disk's center of mass is located a distance d above the reference axis of the shaft, thereby creating an unbalance of the system.

Table 4 Sectional stiffness properties of the shaft

Axial S [MN]	Shearing K_{22} [MN]	Shearing K_{33} [MN]	Torsional H_{11} [kN m ²]	Bending H_{22} [kN m ²]	Bending H_{33} [kN m ²]
313.4	60.5	60.5	272.7	354.5	354.5

At the initial time, the shaft is at rest and deformed under the effect of the gravity loads acting in the vertical direction, as indicated in the figure. The shaft is set in motion by prescribing its rotation at point **R** and lateral oscillations ensue due to the initial imperfection of the system. As the shaft accelerates, it passes through the first natural bending frequency of the system and the operation goes from sub- to super-critical. As predicted by linear rotor dynamics theory, the shaft becomes unstable when operating at the critical speed. In the present example, the magnitudes of lateral oscillations and corresponding internal forces rise as the shaft is accelerated through the critical speed.

The shaft has a length $L = 6$ m and is made of steel (density $\rho = 7800$ kg/m³, Young’s modulus $E = 210$ GPa, and Poisson’s ratio $\nu = 0.3$). The cross-section is annular with inner and outer radii $r_I = 0.045$ and $r_O = 0.05$ m, respectively. The shaft’s sectional stiffness properties are summarized in Table 4. The mass per unit span is $m = 11.64$ kg/m, the moments of inertia per unit span are $m_{22} = m_{33} = 13.17$ g m²/m and the resulting polar moment of inertia per unit span is $m_{11} = m_{22} + m_{33} = 26.34$ g m²/m.

The mid-span circular disk is of mass $m_d = 70.573$ kg, radius $r_d = 0.24$ m, and thickness $t_d = 0.05$ m. Its inertial tensor computed with respect to the center of mass is diagonal, diag(2.0325, 1.0163, 1.0163) g m². Its center of mass is located a distance $d = 0.05$ m above the shaft reference axis. The acceleration of gravity is $g = 9.81$ m/s².

The shaft’s rotation at point **R** is prescribed to be

$$\Omega(t) = \begin{cases} A_1\omega[1 - \cos(\pi t/T_1)]/2, & 0 \leq t \leq T_1, \\ A_1\omega, & T_1 < t \leq T_2, \\ A_1\omega + (A_2 - A_1)\omega\{1 - \cos[\pi(t - T_2)/(T_3 - T_2)]\}/2, & T_2 < t \leq T_3, \\ A_2\omega, & t > T_3, \end{cases} \quad (3)$$

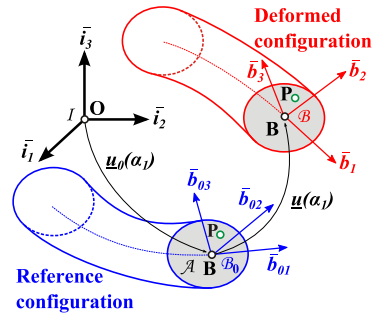
where $A_1 = 0.8$, $A_2 = 1.2$, $T_1 = 0.5$ s, $T_2 = 1$ s, $T_3 = 1.25$ s, and $\omega = 60$ rad/s is close to the first natural frequency of the shaft in bending ($\omega_1 = 56.7$ rad/s).

3 General description of beam formulations

A beam is defined as a structure having one of its dimensions much larger than the other two, as depicted in Fig. 5. The axis, or reference line, of the beam is defined along that longer dimension and its cross-section is normal to this axis. The cross-section’s geometric and physical properties are assumed to vary smoothly along the beam’s span.

Figure 5 depicts an initially curved and twisted beam of length L , with a cross-section of arbitrary shape and area \mathcal{A} . The volume of the beam is generated by sliding the cross-section along the reference line of the beam, which is defined by an arbitrary curve in space. Curvilinear coordinate α_1 defines the intrinsic parameterization of this curve, i.e., it measures length along the beam’s reference line. Point **B** is located at the intersection of the reference line with the plane of the cross-section.

Fig. 5 Curved beam in the reference and deformed configurations



3.1 Kinematics of the problem

In the reference configuration, an orthonormal basis, $\mathcal{B}_0(\alpha_1) = (\bar{b}_{01}, \bar{b}_{02}, \bar{b}_{03})$, is defined at point \mathbf{B} . Vector \bar{b}_{01} is the unit tangent vector to the reference curve at that point, and unit vectors \bar{b}_{02} and \bar{b}_{03} define the plane to the cross-section. An inertial reference frame, $\mathcal{F}_I = [\mathbf{O}, \mathcal{I} = (\bar{i}_1, \bar{i}_2, \bar{i}_3)]$, is defined, and the components of the rotation tensor that brings basis \mathcal{I} to \mathcal{B}_0 , resolved in basis \mathcal{I} , are denoted $\underline{\underline{R}}_0(\alpha_1)$.

The position vector of point \mathbf{B} along the beam's reference line is denoted $\underline{u}_0(\alpha_1)$. The position vector of material point \mathbf{P} of the beam then becomes $\underline{x}(\alpha_1, \alpha_2, \alpha_3) = \underline{u}_0(\alpha_1) + \alpha_2 \bar{b}_{02} + \alpha_3 \bar{b}_{03}$, where α_2 and α_3 are the material coordinates along unit vectors \bar{b}_{02} and \bar{b}_{03} , respectively. Coordinates α_1, α_2 , and α_3 form a natural choice of coordinates to represent the configuration of the beam.

In the deformed configuration, all material points located on a cross-section of the beam move to new positions. This motion is decomposed into two parts, a rigid-body motion and a warping displacement field. The rigid-body motion consists of a translation of the cross-section, characterized by displacement vector $\underline{u}(\alpha_1)$ of reference point \mathbf{B} , and of a rotation of the cross-section, which brings basis \mathcal{B}_0 to $\mathcal{B}(\alpha_1) = (\bar{b}_1, \bar{b}_2, \bar{b}_3)$, see Fig. 5. The components of the position vector of point \mathbf{B} in the deformed configuration are denoted $\underline{x}(\alpha_1)$ and the components of the rotation tensor that brings basis \mathcal{B}_0 to \mathcal{B} are denoted $\underline{\underline{R}}(\alpha_1)$; all tensor components are resolved in basis \mathcal{I} .

For shear deformable beams, the deformation is characterized by six sectional strains: the axial strain, the two transverse shear strains, the twist rate, and the two bending curvatures.

3.2 Definition of the sectional strain

In the GEBF, the geometry of the beam is described by the displacement field of the beam's reference axis and by the rotation field of its cross-section. The sectional strains and curvatures, denoted $\underline{\underline{\varepsilon}}(\alpha_1)$ and $\underline{\underline{\kappa}}(\alpha_1)$, respectively, are expressed [2] as

$$\underline{\underline{\varepsilon}}(\alpha_1) = \underline{u}'_0 + \underline{u}' - (\underline{\underline{R}}\underline{\underline{R}}_0)\bar{i}_1, \tag{4a}$$

$$\underline{\underline{\kappa}}(\alpha_1) = \text{axial}(\underline{\underline{R}}'\underline{\underline{R}}^T), \tag{4b}$$

where \underline{u}_0 is the position vector of the beam's axis in its reference configuration and notation $(\cdot)'$ denotes a derivative with respect to α_1 . The strain vector is defined as $\underline{\underline{\varepsilon}}^T = \{\varepsilon_{11}, \gamma_{12}, \gamma_{13}\}$, where ε_{11} is the sectional axial strain, and γ_{12} and γ_{13} the two components of transverse shearing strains.

3.3 The strain energy

The strain energy stored in the beam [20] of length L is expressed as

$$A = \frac{1}{2} \int_0^L \underline{\underline{\boldsymbol{\varepsilon}}}^{*T} \underline{\underline{\boldsymbol{C}}}^* \underline{\underline{\boldsymbol{\varepsilon}}}^* d\alpha_1, \tag{5}$$

where array $\underline{\underline{\boldsymbol{\varepsilon}}}^{*T} = \{\underline{\underline{\boldsymbol{\varepsilon}}}^{*T}, \underline{\underline{\boldsymbol{\kappa}}}^{*T}\}$ stores the beam’s sectional strain components resolved in material basis \mathcal{B} , i.e., $\underline{\underline{\boldsymbol{\varepsilon}}}^* = (\underline{\underline{\boldsymbol{R}}}\underline{\underline{\boldsymbol{R}}}_0)^T \underline{\underline{\boldsymbol{\varepsilon}}}$ and $\underline{\underline{\boldsymbol{\kappa}}}^* = (\underline{\underline{\boldsymbol{R}}}\underline{\underline{\boldsymbol{R}}}_0)^T \underline{\underline{\boldsymbol{\kappa}}}$. If the beam’s cross-section is made of isotropic materials and characterized by double symmetry, the sectional stiffness matrix referred to the centroid of the section is diagonal, $\underline{\underline{\boldsymbol{C}}}^* = \text{diag}(S, K_{22}, K_{33}, H_{11}, H_{22}, H_{33})$, where S is the beam’s axial stiffness, K_{22} and K_{33} its shear stiffnesses along unit vectors \bar{b}_2 and \bar{b}_3 , respectively, H_{11} its torsional stiffness, and H_{22} and H_{33} its bending stiffnesses about unit vectors \bar{b}_2 and \bar{b}_3 , respectively.

3.4 Equilibrium equations

The sectional forces and moments resolved in basis \mathcal{I} are denoted $\underline{\underline{\boldsymbol{N}}}$ and $\underline{\underline{\boldsymbol{M}}}$, respectively. When rotated to material basis \mathcal{B} , the corresponding quantities are denoted $\underline{\underline{\boldsymbol{N}}}^*$ and $\underline{\underline{\boldsymbol{M}}}^*$, respectively where $\underline{\underline{\boldsymbol{N}}}^{*T} = \{N_1^*, V_2^*, V_3^*\}$ and $\underline{\underline{\boldsymbol{M}}}^{*T} = \{M_1^*, M_2^*, M_3^*\}$. The sectional axial force is N_1^* , and V_2^* and V_3^* are the shear forces along unit vector \bar{b}_2 and \bar{b}_3 , respectively. Finally, M_1^* is the torque, and M_2^* and M_3^* are the bending moments about unit vector \bar{b}_2 and \bar{b}_3 , respectively. Array $\underline{\underline{\boldsymbol{F}}}^{*T} = \{\underline{\underline{\boldsymbol{N}}}^{*T}, \underline{\underline{\boldsymbol{M}}}^{*T}\}$ stores the six sectional stress resultants and the sectional constitutive laws are $\underline{\underline{\boldsymbol{F}}}^* = \underline{\underline{\boldsymbol{C}}}^* \underline{\underline{\boldsymbol{\varepsilon}}}^*$.

Application of the principle of virtual work then yields the static equilibrium equations of the problem

$$\underline{\underline{\boldsymbol{N}}}' = -\underline{\underline{\boldsymbol{f}}}, \tag{6a}$$

$$\underline{\underline{\boldsymbol{M}}}' + (\bar{b}_1 + \underline{\underline{\boldsymbol{u}}}') \times \underline{\underline{\boldsymbol{N}}} = -\underline{\underline{\boldsymbol{m}}}, \tag{6b}$$

where $\underline{\underline{\boldsymbol{f}}}$ and $\underline{\underline{\boldsymbol{m}}}$ denote the externally applied forces and moments per unit span of the beam, respectively.

4 Description of the codes used in this effort

This paper will present the predictions of eight different codes for the four benchmark problems introduced in Sect. 2. These eight codes are described in the present section in a very succinct manner. Table 5 lists the eight codes and the references providing details about them. Clearly, the details of the finite element implementation of each of the formulations are beyond the scope of this paper.

Description of Dymore Dymore is based on the geometrically exact beam formulation. The sectional strains are defined by Eqs. (4a), (4b) and the strain energy by Eq. (5). The results presented in this paper use a four-node element based on cubic Lagrangian shape functions. Each node features six degrees of freedom (DOFs), three displacement components and three rotation components. The Wiener–Milenković [22] parameters are used to represent finite rotations. A complete description of the formulations is found in [21, 22].

Table 5 Summary of the codes used for the numerical predictions

Code name	Symbol	References
Dymore	*	[21, 22]
Hotint	○	[23]
MBDyn	△	[24, 25]
Mecano	▽	[12, 26]
MOPEDS	□	[27, 28]
Oofelie	×	[29, 30]
SE(3)	+	[31, 32]
Spacar	◇	[33, 34]

Description of Hotint HOTINT (<http://www.hotint.org>) is an open source multibody dynamics simulation code which has been developed at the Johannes Kepler University Linz and at the Linz Center of Mechatronics. HOTINT includes various possibilities for the modeling of point masses, rigid bodies, beams, plates, and modally reduced multibody systems. The beam formulation is based on the ANCF described by Nachbagauer et al. [23]. The nodal coordinates are given by a displacement vector and two slope vectors, which coincide with the principal axes of the cross-section in the reference configuration. As these two slope vectors are not necessarily perpendicular (but they are nearly) during deformation of the beam, a modification of constraints, moments and sensors which are related with the rotation of the cross-section is performed. Thus, for the computation of the rotation matrix from the two slope vectors in any point at the beam axis, a Gram–Schmidt projection of the slope vectors is utilized in order to obtain rotational parameters as provided in the results. The multibody system is represented by means of a differential algebraic equations of index 3, which is solved by means of a RadauIIA scheme with two stages (order 3) to provide numerical damping.

Description of MBDyn The structural DOFs used by MBDyn are the absolute position of the nodes in reference \mathcal{I} and the Cayley–Gibbs–Rodrigues [22] parameters which are used to represent finite rotations. The approach uses an incremental scheme that resembles an updated Lagrangian approach which has been termed *updated–updated* [24]. The constrained dynamics problem is formulated as DAEs that express Newton–Euler’s equations of motion of rigid bodies connected by deformable components and subjected to kinematic constraints in form of algebraic equations. It is integrated using an implicit, A/L stable multistep scheme with tunable algorithmic dissipation [24].

MBDyn supports GEBF elements implemented according to the finite-volume approach developed by Ghiringhelli et al. [25]. The generalized strains are defined according to Eqs. (4a), (4b). Integration by parts of the equilibrium equations (6a), (6b), weighted by piecewise constant test functions centered on the nodes, yields the elastic contribution to the equilibrium of naturally discrete pieces of beam. When a three-node discretization is considered, with the interfaces between the mid- and the end-nodes at points corresponding to the two Gauss quadrature points, an intrinsically shear-locking free discrete element is obtained, which yields the exact static solution for any end-applied node. Inertia loads are accounted for using rigid-body elements at the nodes.

Description of Mecano Mecano includes a large rotation nonlinear finite element beam based on the static equilibrium equations (6a), (6b) resolved in the material frame [12, 26]. Rotations are parameterized using the rotational vector [22] and an updated Lagrangian

scheme allows the handling of rotation in excess of 2π in magnitude. The element fields are interpolated linearly within the element and a single Gauss point is used for integration. To enable large finite rotations, incremental rotations with respect to the previous converged configuration are interpolated. This scheme requires tracking of total rotations both at the element nodes and at the Gauss point. This code, which is part of the LMS Samtech-SAMCEF software, has been used in industrial applications extensively for the last 20 years.

Description of MOPEDS The beam finite element is based on the GEBF described in Sects. 3.1 to 3.4. The finite element formulation relies on standard Lagrangian shape functions used for the interpolation of the beam reference line, $\underline{u}_0(\alpha_1) + \underline{u}(\alpha_1)$, and the rotation tensor, $\underline{R}(\alpha_1)\underline{R}_0(\alpha_1)$. The orthogonality of the rotation tensor is relaxed to the nodal points of the finite element. To this end, either Lagrangian multipliers or three (incremental) rotations are employed. Details of the finite element formulation can be found in Betsch and Steinmann [27]. The incorporation of the beam finite element formulation into a general framework for flexible multibody dynamics is described by Leyendecker et al. [28]. It is worth noting that the present approach makes possible the design of energy–momentum consistent time integrators. A refined version of the beam finite element formulation exhibiting improved convergence properties has recently been proposed by Eugster et al. [35].

Description of Oofelie A large rotations nonlinear beam finite element model was developed by Lens and Cardona [29]. The finite element is able to handle large three-dimensional rotations and displacements but is restricted to small strains. Simplifications are made in the kinematics that allowed to obtain quite simple compact expressions. The kinematics expressions are based on assuming small relative displacements and rotations within the element. A single Gauss point is used to compute the strain energy and the expressions of rotations at the middle point are computed using a multiplicative decomposition of the increment of rotation from one node to the other. Then, curvatures and strains are obtained by assuming simple approximations for the derivative of the rotation tensor with respect to the axial coordinate, evaluated at the middle point. Full analytical expressions of the internal forces, inertia forces, stiffness, and mass matrices can be obtained, allowing an easy implementation of the element. The element was implemented in the finite element code Oofelie [30], which is being developed jointly by the University of Liège, the Universidad Nacional del Litoral and the company Open Engineering S.A.

Description of formulation in the special Euclidean group The kinematics of mechanical systems are described using frame transformations which are treated as elements of the special Euclidean group $SE(3)$. Brüls et al. [36] used this approach to simulate rigid bodies. Generalizations to kinematic joints and beam elements were proposed by Sonnevile and Brüls [31] and Sonnevile et al. [32]. The constraint equations and the internal and inertia forces are naturally expressed in terms of unknowns evaluated in the material frame, and hence, the tangent matrix depends on local relative motions only and remains constant under rigid-body motions. By construction, the formulation is frame invariant. The equations of motion take the form of second-order differential-algebraic equations on a Lie group and are solved using a Lie group time integration scheme, the generalized- α method proposed by Brüls et al. [36].

In the beam formulation, a material frame is attached to each point of the neutral axis of the beam, accounting for the position of the point and the orientation of the cross-section at that point with respect to the inertial frame. A two-node element is used and the finite element interpolation of the nodal frames is based on the exponential map of the special Euclidean group $SE(3)$. The resulting shape functions are helicoidal functions and the coupling between rotations and translations they introduce yields a naturally locking-free element.

Description of Spacar Spacar is based on the generalized strain beam formulation of Besseling [37] (<http://www.utwente.nl/ctw/wa/software/spacar>). A key point in this formulation is the selection of generalized strains as discrete deformations that are invariant for rigid-body motions of the element. The deformations are expressed as analytical functions of the absolute nodal coordinates in a co-rotational framework. The deformation functions include the specification of rigid body motions as displacements for which the discrete deformations are zero. This avoids the shortcoming of standard co-rotational formulations when describing rigid bodies. Flexible elements are handled by allowing nonzero deformations and specifying constitutive relations between the discrete deformations and stress-resultants. The derivation of the element stiffness matrix is based on a discretization of the elastic line of a three-dimensional Timoshenko beam model in a co-rotational frame, whereas the inertia properties are derived using a discretization of the elastic line in the inertial frame of reference.

Geometric nonlinearities arising from changes in geometry involving finite deflections and pre- and post-buckling, are approximated by additional second-order terms in the expressions for the deformations. These second-order terms are derived from a nonlinear continuum model of the elastic line in the co-rotational frame, including a finite strain description proposed by Reissner [38]. A Taylor series expansion is used to express the nonlinear curvature and strain displacement equations into a second-order polynomial. Integrating these equations over the length of the beam and using the second moment–area theorem yields the additional second-order terms describing the geometric couplings among the axial elongation, bending, and torsion deformations. A detailed description of the formulation is found in Jonker et al. [33, 34].

5 Comparison of numerical predictions

In this section, the numerical predictions of the beam formulations described in Sects. 3 and 4 will be compared for the four benchmark problems listed in Sect. 2. The first and second columns of Table 5 lists the name of the formulations and the symbol that will be used to identify the numerical predictions of each code.

5.1 The Princeton beam experiment

In this correlation effort, the distributed weight of the beam was neglected. Unit vector \bar{b}_3 , see Fig. 1, was left in the vertical orientation and the orientation of the tip load was rotated from 0 to 90 degrees. While this represents an approximation, its effect on the numerical predictions is far smaller than the observed scatter in the experimental measurements.

Figures 6, 7, and 8 show the tip flapwise displacement, u_2 , chordwise displacement, u_3 , and twist, ϕ , respectively. The experimental measurements (average \bigcirc and error bars) for each of the three loading cases, labeled P_1 , P_2 , and P_3 , respectively, are shown in the figures. The numerical predictions of the eight codes presented in Sect. 4 are also shown, using the symbols listed in Table 5. For reference, the linear solution given by Eqs. (2) is also shown in Figs. 6 and 7 with dotted lines; the linear solution predicts a vanishing tip twist. The tip rotation is the quantity most affected by nonlinear behavior. The eight predictions of the maximum values of the tip rotation for load case P_3 were averaged to find $\mu_\phi = 0.06177$ rad and the coefficient of variation was $\sigma_\phi/\mu_\phi = 0.0076$, where σ_ϕ is the standard deviation of the distribution. Clearly, the predictions of the eight codes are in very close agreement.

Fig. 6 Tip flapwise displacement vs. loading angle for three loading conditions

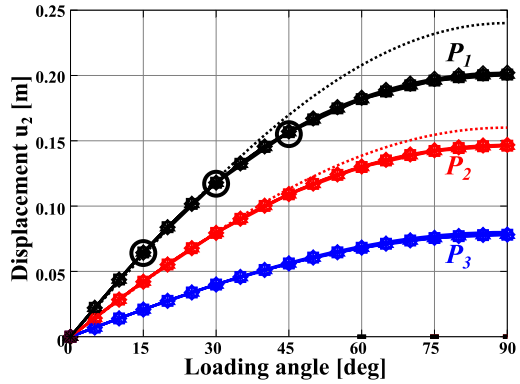


Fig. 7 Tip chordwise displacement vs. loading angle for three loading conditions

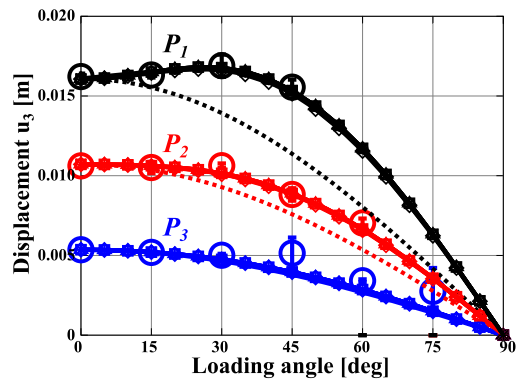
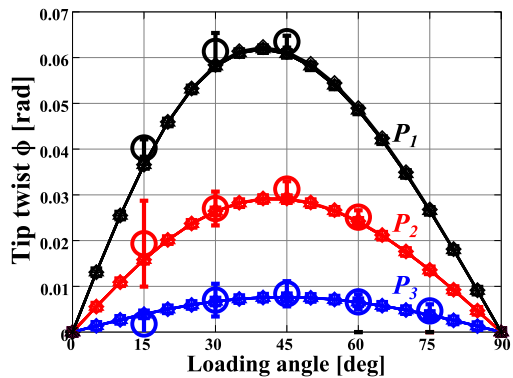


Fig. 8 Tip twist vs. loading angle for three loading conditions



Note that the Dowell and Traybar report [18] provides no measurements for loading condition P_2 at loading angles $\theta = 75$ and 90 degrees and for loading condition P_3 at loading angles $\theta = 60, 75,$ and 90 degrees. A cursory look at Fig. 6 reveals that those loading cases would result in large flapwise deflections, which could generate permanent plastic deformations in the beam. It is likely that the authors of the study did not want to damage the test article, and hence did not acquire data at those loading conditions.

Fig. 9 Axial force, F_1 , at the mid-span of bar 1

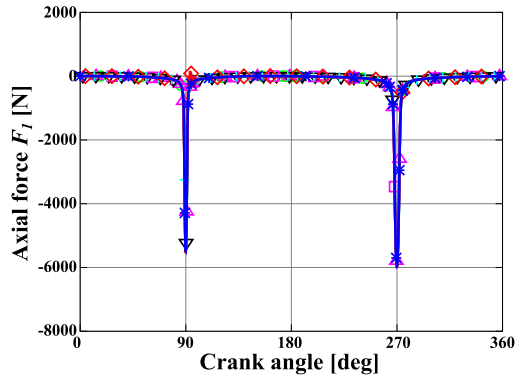
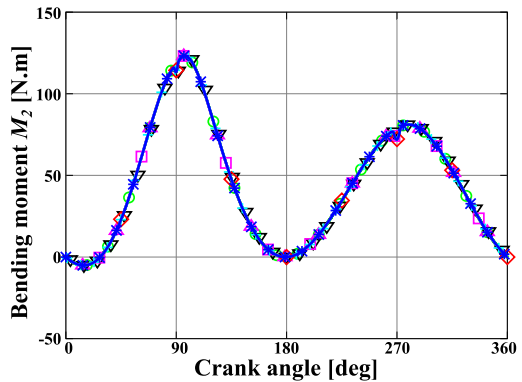


Fig. 10 Bending moment, M_2 , at the mid-span of bar 1



5.2 The four-bar mechanism

For this problem, the simulation was run for three complete revolutions of the crank, starting from initial conditions at rest. At the beginning of the first revolution, high-frequency oscillations are observed, but due to the algorithmic dissipation, these oscillations have all but disappeared in the second revolution. The results presented in the sequel are the numerical predictions for the third revolution. This problem was simulated for a total of 12 s using 3000 time steps of constant size $\Delta t = 4$ ms.

The components of axial force, F_1 , and bending moment, M_2 , along unit vector \bar{b}_1 and about unit vector \bar{b}_2 , respectively, at the mid-span of bar 1, both resolved in the material basis are depicted in Figs. 9 and 10, respectively. The component of rotation of bar 2 at point C, φ , is shown in Fig. 11. At point C, the Euler angles (sequence 3-1-2) defining the orientation of bar 2 in the inertial basis are computed and the first angle of the sequence is presented in the figure. The relative rotation, θ , at the revolute joint at point D is depicted in Fig. 12. The predictions of the eight codes are shown using the symbols listed in Table 5.

The four figures show that the predictions of the eight codes are in excellent agreement with each other. To quantify the quality of the agreement, the eight predictions of the minimum values of the axial force shown in Fig. 9 were averaged to find $\mu_{F_1} = -5966$ N and the coefficient of variation was $\sigma_{F_1}/\mu_{F_1} = 0.0043$, where σ_{F_1} is the standard deviation of the distribution. Clearly, the predictions of the eight codes are in very close agreement. Similarly, the average of the eight maximum relative rotations at point D appearing in

Fig. 11 Rotation, φ , at the tip of bar 2 at point C

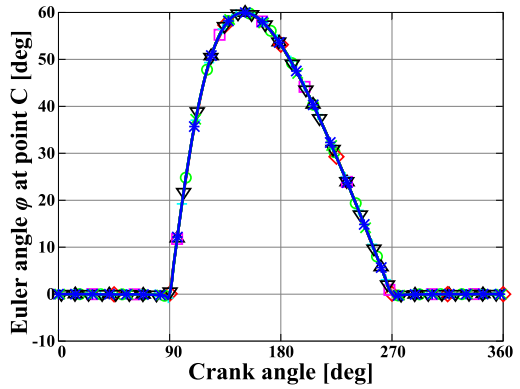


Fig. 12 The relative rotation, θ , at the revolute joint at point D

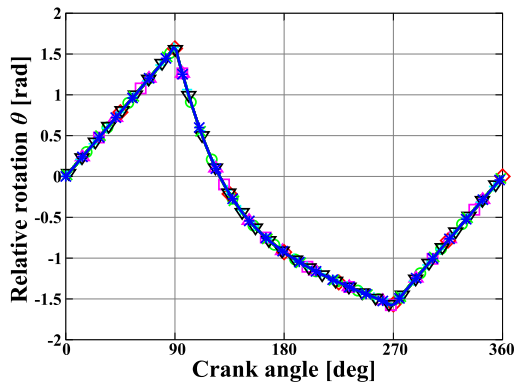


Fig. 13 Displacement u_2 at the beam's mid-span

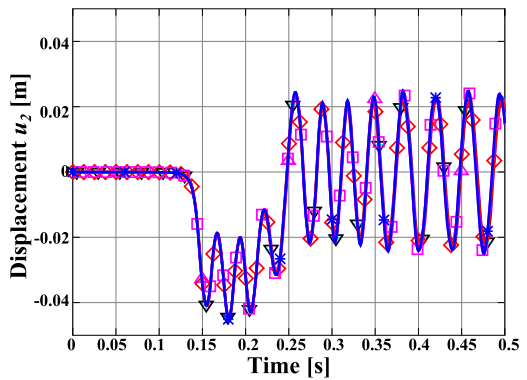


Fig. 12 was found to be $\mu_\theta = 1.579$ rad and the corresponding coefficient of variation was $\sigma_\theta / \mu_\theta = 0.0032$.

5.3 Lateral buckling of a thin beam

For this problem, the simulation was run for a total of 0.5 s. The beam quickly buckles laterally, generating violent oscillations that continue after the crank has stopped in the 180

Fig. 14 Angular velocity ω_1 at the beam's mid-span

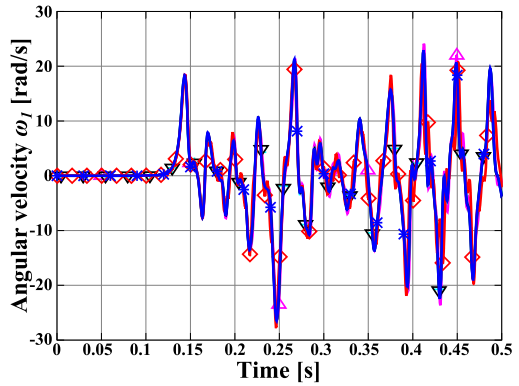


Fig. 15 Shear force F_3 at the beam's mid-span

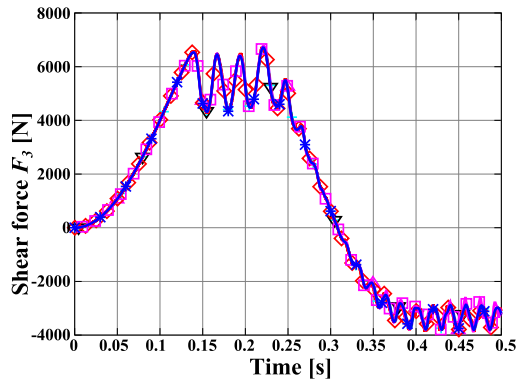
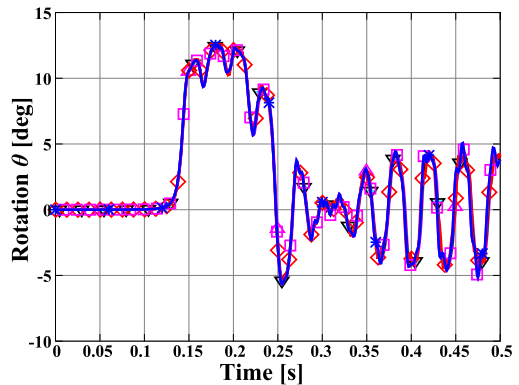


Fig. 16 Rotation θ at the beam's mid-span



degree position at time $t = 0.4$ s. Figures 13 and 14 show the component of displacement, u_2 , along unit vector \bar{i}_2 and angular velocity, ω_1 , about unit vector \bar{i}_1 , respectively, at the beam's mid-span. Figure 15 shows the component of transverse shear force, F_3 , along unit vector \bar{e}_3 , resolved in the material basis, at the beam's mid-span. The rotation, θ , at the beam's mid-span was also evaluated: the beam's Euler angles (sequence 3-1-2) in the inertial basis were computed and the second angle of the sequence is presented in Fig. 16.

Fig. 17 Trajectory of shaft's mid-span viewed by inertial observer

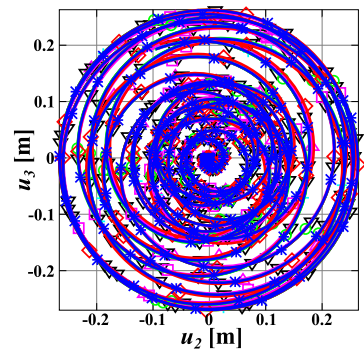
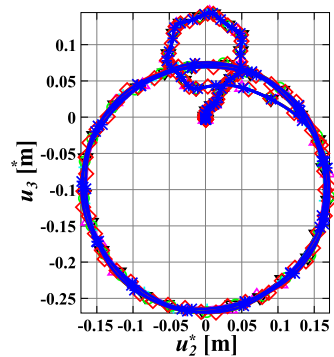


Fig. 18 Trajectory of shaft's mid-span viewed by a rotating observer



Due to the highly oscillatory nature of the response, the time integration process is more arduous. Yet, the agreement among the eight predictions remained excellent. For instance, the eight predictions of the peaks in angular velocity at time $t \approx 0.25$ s were averaged to find $\mu_{\omega_1} = -27.11$ rad/s and the coefficient of variation as $\sigma_{\omega_1} / \mu_{\omega_1} = 0.066$.

5.4 Stability of a rotating shaft

The angular velocity of the shaft was prescribed according to Eq. (3) and the response was simulated for a total time of 2.5 s with a constant time step $\Delta t = 0.1$ ms. The shaft's dynamic response is best illustrated by the trajectory of its mid-span point as viewed by inertial and rotating observers, see Figs. 17 and 18, respectively. Because the shaft operates above its critical speed for time $t > 1.25$ s, it becomes self-centering, explaining the circular trajectory of its geometric center observed by a rotating observer, see Fig. 18.

Figures 19 and 20 show the phase plot of shaft's mid-span for the displacement and velocity components along unit vectors \bar{i}_2 and \bar{i}_3 , respectively. Here again, excellent agreement is observed between the eight codes.

6 Conclusions

This paper has described in details four benchmark problems for the validation of beam models used in flexible multibody dynamics simulations. For each of the four benchmark

Fig. 19 The phase plot of shaft's mid-span for components along unit vector \bar{i}_2

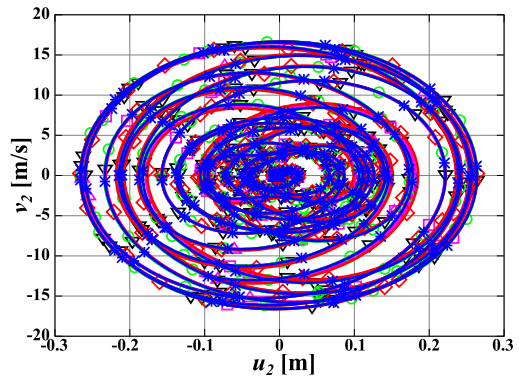
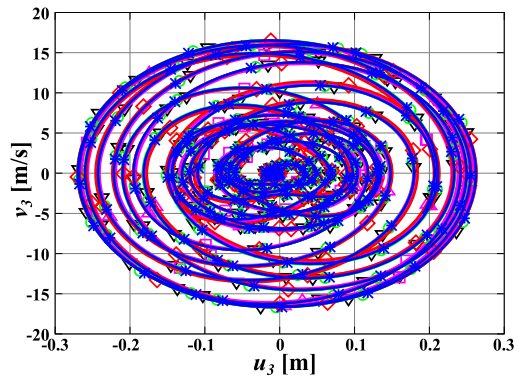


Fig. 20 The phase plot of shaft's mid-span for components along unit vectors \bar{i}_3



problems, the numerical predictions of eight independent codes have been presented and the formulations on which these codes are based have been described succinctly.

Many of the formulations are related closely to the geometrically exact beam formulation but they differ in their finite element implementation, time integration scheme, treatment of the constraints and invariants, and solution techniques. The eight formulations have been implemented by eight researchers independently. Yet, this paper shows that the predictions obtained by the eight researchers are in very good agreement with each other and with experimental results, when available.

Because the proposed benchmark problems have been described accurately and have been run by eight different researchers successfully, they are expected to be useful to other researchers for the validation of future beam element formulations. All the numerical predictions presented in the paper are available in electronic format at <http://www.dymoresolutions.com/Benchmarks/Benchmarks.html>.

The present paper has focused on the consistency of the predictions of eight different codes. The efficiency of these codes, however, has not been assessed. Indeed, assessment of computation efficiency would require the eight codes to be run on the same computer hardware, or at least to evaluate their computational complexity. This difficult issue will have to be addressed in the future to be able to assess both accuracy and efficiency of the various formulations.

Conflict of interest The authors declare that they have no conflict of interest. This article does not contain any studies with human participants or animals performed by any of the authors. Informed consent was obtained from all individual participants included in the study.

References

1. Shabana, A.A.: Flexible multibody dynamics: review of past and recent developments. *Multibody Syst. Dyn.* **1**(2), 189–222 (1997)
2. Simo, J.C.: A finite strain beam formulation. The three-dimensional dynamic problem. Part I. *Comput. Methods Appl. Mech. Eng.* **49**(1), 55–70 (1985)
3. Belytschko, T., Hsieh, B.J.: Nonlinear transient finite element analysis with convected coordinates. *Int. J. Numer. Methods Eng.* **7**, 255–271 (1973)
4. Shabana, A.A., Hussien, H.A., Escalona, J.L.: Application of the absolute nodal coordinate formulation to large rotation and large deformation problems. *J. Mech. Des.* **120**, 188–195 (1998)
5. Escalona, J.L., Hussien, H.A., Shabana, A.A.: Application of the absolute nodal co-ordinate formulation to multibody system dynamics. *J. Sound Vib.* **214**(5), 833–851 (1998)
6. Romero, I.: A comparison of finite elements for nonlinear beams: the absolute nodal coordinate and geometrically exact formulations. *Multibody Syst. Dyn.* **20**, 51–68 (2008)
7. Gerstmayr, J., Sugiyama, H., Mikkola, A.: An overview on the developments of the absolute nodal coordinate formulation. In: *Proceedings of the Second Joint International Conference on Multibody System Dynamics*, Stuttgart, Germany (2012)
8. Bauchau, O.A., Han, S.L., Mikkola, A., Matikainen, M.K.: Comparison of the absolute nodal coordinate and geometrically exact formulations for beams. *Multibody Syst. Dyn.* **32**(1), 67–85 (2014)
9. Bauchau, O.A., Han, S.L., Mikkola, A., Matikainen, M.K., Gruber, P.: Experimental validation of flexible multibody dynamics beam formulations. *Multibody Syst. Dyn.* **34**(4), 373–389 (2015)
10. Hegemier, G.A., Nair, S.: A nonlinear dynamical theory for heterogeneous, anisotropic, elastic rods. *AIAA J.* **15**(1), 8–15 (1977)
11. Hodges, D.H.: A mixed variational formulation based on exact intrinsic equations for dynamics of moving beams. *Int. J. Solids Struct.* **26**(11), 1253–1273 (1990)
12. Cardona, A., Géradin, M.: A beam finite element non-linear theory with finite rotation. *Int. J. Numer. Methods Eng.* **26**, 2403–2438 (1988)
13. Hilber, H.M., Hughes, T.J.R., Taylor, R.L.: Improved numerical dissipation for time integration algorithms in structural dynamics. *Earthq. Eng. Struct. Dyn.* **5**, 283–292 (1977)
14. Betsch, P., Steinmann, P.: Constrained integration of rigid body dynamics. *Comput. Methods Appl. Mech. Eng.* **191**, 467–488 (2001)
15. Celledoni, E., Owren, B.: Lie group methods for rigid body dynamics and time integration on manifolds. *Comput. Methods Appl. Mech. Eng.* **192**(3–4), 421–438 (2003)
16. Bauchau, O.A., Han, S.L.: Three-dimensional beam theory for flexible multibody dynamics. *J. Comput. Nonlinear Dyn.* **9**(4), 041011 (2014), 12 pp.
17. Han, S.L., Bauchau, O.A.: Nonlinear three-dimensional beam theory for flexible multibody dynamics. *Multibody Syst. Dyn.* **34**(3), 211–242 (2015)
18. Dowell, E.H., Traybar, J.J.: An experimental study of the nonlinear stiffness of a rotor blade undergoing flap, lag, and twist deformations. *Aerospace and Mechanical Science Report 1257*, Princeton University (1975)
19. Dowell, E.H., Traybar, J.J., Hodges, D.H.: An experimental-theoretical correlation study of non-linear bending and torsion deformations of a cantilever beam. *J. Sound Vib.* **50**(4), 533–544 (1977)
20. Bauchau, O.A., Craig, J.I.: *Structural Analysis with Application to Aerospace Structures*. Springer, Dordrecht/Heidelberg/London/New-York (2009)
21. Bauchau, O.A., Bottasso, C.L., Nikishkov, Y.G.: Modeling rotorcraft dynamics with finite element multibody procedures. *Math. Comput. Model.* **33**(10–11), 1113–1137 (2001)
22. Bauchau, O.A.: *Flexible Multibody Dynamics*. Springer, Dordrecht/Heidelberg/London/New-York (2011)
23. Nachbagauer, K., Gruber, P., Gerstmayr, J.: Structural and continuum mechanics approaches for a 3D shear deformable ANCF beam finite element: application to static and linearized dynamic examples. *J. Comput. Nonlinear Dyn.* **8**(2), 021004 (2013)
24. Masarati, P., Morandini, M., Mantegazza, P.: An efficient formulation for general-purpose multibody/multiphysics analysis. *J. Comput. Nonlinear Dyn.* **9**(4), 041001 (2014)
25. Ghiringhelli, G.L., Masarati, P., Mantegazza, P.: A multi-body implementation of finite volume beams. *AIAA J.* **38**(1), 131–138 (2000)
26. Cardona, A.: An integrated approach to mechanism analysis. PhD thesis, Université de Liège, Belgium (1989)
27. Betsch, P., Steinmann, P.: Frame-indifferent beam element based upon the geometrically exact beam theory. *Int. J. Numer. Methods Eng.* **54**, 1775–1788 (2002)
28. Leyendecker, S., Betsch, P., Steinmann, P.: The discrete null space method for the energy consistent integration of constrained mechanical systems. Part III: flexible multibody dynamics. *Multibody Syst. Dyn.* **19**(1–2), 45–72 (2008)

29. Lens, E.V., Cardona, A.: A nonlinear beam element formulation in the framework of an energy preserving time integration scheme for constrained multibody systems dynamics. *Comput. Struct.* **86**(1–2), 47–63 (2008)
30. Cardona, A., Klapka, I., G eradin, M.: Design of a new finite element programming environment. *Eng. Comput.* **11**, 365–381 (1994)
31. Sonnevill , V., Br uls, O.: A formulation on the special Euclidean group for dynamic analysis of multibody systems. *J. Comput. Nonlinear Dyn.* **9**(4) (2014)
32. Sonnevill , V., Cardona, A., Br uls, O.: Geometrically exact beam finite element formulated on the special Euclidean group $SE(3)$. *Comput. Methods Appl. Mech. Eng.* **268**(1), 451–474 (2014)
33. Jonker, J.B.: A finite element dynamic analysis of spatial mechanisms with flexible links. *Comput. Methods Appl. Mech. Eng.* **76**, 17–40 (1989)
34. Jonker, J.B., Meijaard, J.P.: A geometrically non-linear formulation of a three-dimensional beam element for solving large deflection multibody system problems. *Int. J. Non-Linear Mech.* **53**, 63–74 (2013)
35. Eugster, S.R., Hesch, C., Betsch, P., Glocker, Ch.: Director-based beam finite elements relying on the geometrically exact beam theory formulated in skew coordinates. *Int. J. Numer. Methods Eng.* **97**(2), 111–129 (2014)
36. Br uls, O., Cardona, A., Arnold, M.: Lie group generalized- α time integration of constrained flexible multibody systems. *Mech. Mach. Theory* **48**, 121–137 (2012)
37. Besseling, J.F.: Non-linear theory for elastic beams and rods and its finite element representation. *Comput. Methods Appl. Mech. Eng.* **12**, 205–220 (1982)
38. Reissner, E.: On one-dimensional large-displacement finite-strain beam theory. *Stud. Appl. Math.* **52**, 87–95 (1973)